

# Investigation of transmission computed tomography (CT) image quality and x-ray dose achievable from an experimental dual-mode benchtop x-ray fluorescence CT and transmission CT system

Luzhen Deng<sup>a,b</sup>, Selcuk Yasar<sup>b</sup>, Md Foiez Ahmed<sup>b</sup>, Sandun Jayarathna<sup>b</sup>, Peng Feng<sup>a</sup>, Biao Wei<sup>a</sup>, Srinivasan Vedantham<sup>c</sup>, Andrew Karellas<sup>c</sup> and Sang Hyun Cho<sup>b,d,\*</sup>

<sup>a</sup>*Key Laboratory of Optoelectronics Technology & System, Chongqing University, Ministry of Education, Chongqing, China*

<sup>b</sup>*Department of Radiation Physics, The University of Texas MD Anderson Cancer Center, Houston, TX, USA*

<sup>c</sup>*Department of Medical Imaging, University of Arizona, Tucson, AZ, USA*

<sup>d</sup>*Department of Imaging Physics, The University of Texas MD Anderson Cancer Center, Houston, TX, USA*

Received 4 October 2018

Revised 8 January 2019

Accepted 3 February 2019

## Abstract.

**OBJECTIVE:** To investigate the image quality and x-ray dose associated with a transmission computed tomography (CT) component implemented within the same platform of an experimental benchtop x-ray fluorescence CT (XFCT) system for multimodal preclinical imaging applications.

**METHODS:** Cone-beam CT scans were performed using an experimental benchtop CT + XFCT system and a cylindrically-shaped 3D-printed polymethyl methacrylate phantom (3 cm in diameter, 7 cm in height) loaded with various concentrations (0.05–1 wt. %) of gold nanoparticles (GNPs). Two commercial CT quality assurance phantoms containing 3D line-pair (LP) targets and contrast targets were also scanned. The x-ray beams of 40 and 62 kVp, both filtered by 0.08 mm Cu and 0.4 mm Al, were used with 17 ms of exposure time per projection at three current settings (2.5, 5, and 10 mA). The ordered-subset simultaneous algebraic reconstruction and total variation–minimization methods were used to reconstruct images. Sparse projection and short scan were considered to reduce the x-ray dose. The contrast-to-noise ratio (CNR) and modulation transfer function (MTF) were calculated.

**RESULTS:** The lowest detectable concentration of GNPs (CNR > 5) and the highest spatial resolution (per MTF50%) were 0.10 wt. % and 9.5 LP/CM, respectively, based on the images reconstructed from 360 projections of the 40 kVp beam (or x-ray dose of 3.44 cGy). The background noise for the image resulting in the lowest GNP detection limit was 25 Hounsfield units.

\*Corresponding author: Sang Hyun Cho. E-mail: scho@mdanderson.org.

**CONCLUSION:** The transmission CT component within the current experimental benchtop XFCT system produced images deemed acceptable for multimodal (CT + XFCT) imaging purposes, with less than 4 cGy of x-ray dose.

Keywords: Computed tomography, x-ray fluorescence computed tomography, x-ray dose, image resolution

## 1. Introduction

Benchtop x-ray fluorescence computed tomography (XFCT) is an emerging quantitative imaging modality in which XFCT, a traditionally synchrotron x-ray imaging modality, is implemented using polychromatic diagnostic x-ray sources [1]. Compared with synchrotron XFCT and other quantitative imaging modalities, benchtop XFCT offers a number of distinct advantages such as easy access and low-cost instrumentation and operation. It also provides unique multimodal/multiplexed *in vivo* imaging capability, when performed with transmission CT (referred to simply as CT throughout the current article), simultaneously or sequentially, within the same platform and various metal probes such as gold nanoparticles (GNPs). A dual mode CT + XFCT system can allow for seamless molecular imaging without relying on radiotracers. This is done through XFCT in conjunction with bioconjugated/functionalized nanoparticles (NPs), while providing anatomical details via CT.

One of the technical challenges for a combined CT + XFCT scan is to minimize x-ray dose, because XFCT scan typically requires a significantly higher x-ray dose than CT imaging. For example, our experimental benchtop XFCT setup would require an x-ray dose on the order of 10 cGy, up to 50 cGy, to image a small animal-sized object (e.g., 3 cm in diameter and 5 cm in height) loaded with a biologically relevant concentration of GNPs ( $\sim 0.1$  wt. %). Thus, the amount of x-ray dose required for XFCT is roughly similar to that required for earlier generations of microCT [2–4]. This means that, if CT and XFCT were performed sequentially (or separately), a combined CT + XFCT scan would double the x-ray dose, which may not be desirable for small animal imaging.

In principle, it is possible to perform a combined CT + XFCT scan simultaneously within the same platform without any extra x-ray dose for CT. However, this approach poses some technical challenges because the optimal operating conditions, particularly the spectrum of x-rays, for XFCT may be significantly different from those for CT. For example, in the case of GNP-based benchtop XFCT utilizing gold K-shell x-ray fluorescence (XRF) photons, we have used the 125 kVp x-ray beam filtered by 1.8 mm of tin for optimal XFCT performance. As shown in our previous study [5], this type of beam does not generate good contrast in CT due to its high energy. Even so, it is still worth investigating ways that may improve CT image quality with such high energy x-ray beams optimized for XFCT. Meanwhile, a practical alternative is to use lower kVp (or energy below the gold K-edge) x-ray beams typically used for microCT imaging, as long as it does not significantly increase the overall x-ray dose. Considering the level of typical x-ray dose required for XFCT and the latest microCT studies, a separate CT scan would be well justified, if it required only a minimal level of x-ray dose (e.g., on the order of 1 cGy or less).

In conventional CT, x-ray dose reduction can be achieved by optimizing the x-ray spectrum or reducing the number of projections or both, while effectively managing the increased image noise or decreased contrast-to-noise ratio (CNR) [6, 7]. Clearly, the key issue for these approaches is to balance the trade-off between noise (or image quality) and x-ray dose. In the current study, we investigated the CT image quality as well as the delivered x-ray dose under various operating conditions suitable for CT scans of small animals—two different x-ray tube voltages (40 and 62 kVp) and three different current levels (2.5, 5 and 10 mA)—using our experimental cone-beam CT + XFCT system. We also investigated two different approaches based on the sparse scan and short scan [8–10] to reduce the

number of projections, while not degrading the image quality significantly. For sparse scan, total variation (TV) minimization [11, 12], based on compressed sensing [13], was used because of its simplicity and efficiency. Short scan was performed with the minimal required data set of  $180^\circ$  plus the fan angle.

The current investigation attempted to provide important quantitative information regarding the CT image quality and x-ray dose associated with our latest experimental cone-beam CT + XFCT system [14]. Especially, this study investigated the feasibility of performing a separate (or sequential) CT scan with a minimal level of x-ray dose, while providing CT image quality deemed acceptable for multimodal (CT + XFCT) preclinical imaging. A thorough investigation for this feasibility also addressed a practical concern regarding our latest experimental cone-beam CT + XFCT system adopting a high power industrial x-ray source with considerably large focal spot sizes (1 or 5.5 mm corresponding to 640 or 3000 W, respectively) [14]. Compared with our previous system utilizing a low power ( $\sim 50$  W) micro-focus ( $< \sim 100 \mu\text{m}$  of focal spot size) x-ray source [1], our latest system, especially under the maximum power setting (i.e., 3000 W and 5.5 mm focal spot size), enabled much faster XFCT scan as well as further optimization of the incident x-ray spectrum. On the other hand, this system resulted in apparent degradation of CT image quality, even with the use of a 1 mm focal spot size at a lower power setting. Thus, it was necessary to ensure that our latest system could produce CT images showing reasonable anatomical details for multimodal (CT + XFCT) preclinical imaging, while meeting the dose constraint for a separate CT scan. Overall, the present study could provide valuable insights into the development of effective strategies to perform combined CT + XFCT scans for preclinical imaging studies using a dual-mode CT + XFCT system.

## 2. Materials and methods

### 2.1. Benchtop CT + XFCT system

Figure 1 shows the experimental benchtop cone-beam CT + XFCT system used for the current investigation. A unipolar tungsten (W)-target x-ray source (MXR-160/22, COMET) with the focal size of 1 mm (DIN EN 12543) was used to generate the incident beam, which was collimated using a cone-beam collimator (made of 5 cm thick lead) with a 1 cm aperture for the entrance and 2 cm aperture

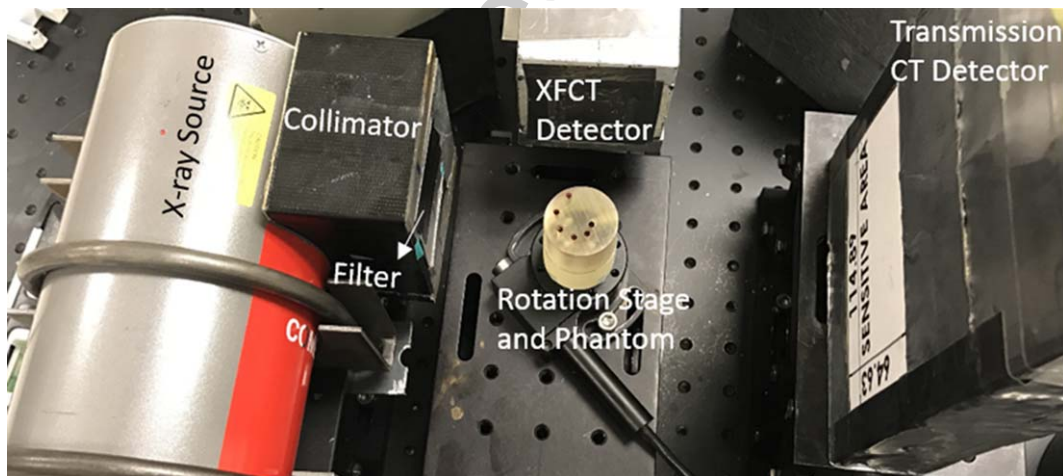


Fig. 1. Setup of the experimental benchtop cone-beam CT + XFCT system. A custom-made cylindrically shaped 3D-printed PMMA phantom with six GNP-loaded columns is also shown.

for the exit. The x-ray beams used for this study (40 and 62 kVp) were filtered using 0.4 mm Al and 0.08 mm Cu in addition to inherent 0.8 mm beryllium x-ray tube window. Phantoms were placed on the rotational stage, which was positioned 150 mm away from the W-target, where the incident beam coverage was more than 3 cm. X-rays transmitting through the phantom were detected using a Dexela x-ray detector (1207NDT with a cesium-iodide scintillator option & 74.8  $\mu\text{m}$  detector pixel pitch). The distance from the phantom center to the transmission CT detector was 115 mm. The XFCT detector was placed at 90° with respect to the incident beam axis. While not used in the current study, this detector allows for XFCT that can be combined with CT for multimodal (CT + XFCT) imaging. More details about the current CT + XFCT system can be found elsewhere [14, 15].

## 2.2. Phantoms

A custom-made cylindrically shaped 3D-printed polymethyl methacrylate phantom (PMMA) (3 cm in diameter, 7 cm in height) containing six spirally placed (clockwise) columns (2 mm in diameter) loaded with various concentrations of GNPs was used. GNP solutions (AuroVist 15 nm; Nanoprobe, Inc., USA) were prepared in phosphate-buffered saline at various concentrations (0.05, 0.08, 0.1, 0.2, 0.5, and 1 wt. %) using a serial dilution method from a stock GNP solution (4 wt. %).

Cylindrically shaped commercial CT imaging quality assurance (QA) phantoms (3.81 cm in diameter, 5.08 cm in height; Model 700-QA, CIRS) were also scanned: 1) a resolution phantom containing 3D line-pair (LP) targets (6, 8, 10, 11, and 12 LP/CM), and 2) a low-contrast phantom containing cylindrical targets (10 and 20 Hounsfield units, HU, above the background).

## 2.3. Data acquisition

The phantom was scanned with 360 projections (ranging from 0 to 359° with 1° increment) of each x-ray beam (40 or 62 kVp) and an exposure time of 17 ms per projection. The x-ray tube current was 10 mA for both 40 and 62 kVp scans. For 40 kVp scans, two additional x-ray tube currents (2.5 and 5 mA) were also used.

## 2.4. Short scans and sparse scans

For fan-beam geometry, 180° plus the fan angle is sufficient [8–10] and commonly referred to as short-scan. Equation (1) describes the relationship among projections:

$$p_{mj} = p_{m+180+a, J-j} \quad (1)$$

where  $p_{m,j}$  is the projection at the  $m$ th angle and  $j$ th detector position ( $J$  is the total size of detector) and  $a = \theta - 2j/J$  ( $\theta$  is the fan angle).

Sparse scan was achieved by reducing the projections to one-half and one-quarter of the total number of projections used in the full scan. Equally spaced projections were selected from the total projections and spaces were 2 and 4 for the half and quarter projections, respectively.

## 2.5. Data processing and reconstruction method

All projections were flat-field corrected and pre-processed (log-normalization) using air scans. Image reconstruction and analysis were implemented in MATLAB R2014b on a computer with the Intel Core i5-4590 CPU running at 3.30 GHz, RAM running at 8.00 GB, and a 64-bit operating system. The central rows of the raw data encompassing the objects (phantoms) were extracted from each projection to generate the sinogram. A Butterworth filter (order was 1 and the cut-off frequency was  $12/J$ ) was

used to filter vertical linear artifacts in the sinogram. The voxel size during image reconstruction was matched with the size of a detector pixel pitch.

In this paper, the ordered-subset simultaneous algebraic reconstruction technique (OS-SART) [16] alone and OS-SART with TV-minimization[11, 12] were applied for reconstruction. Note the former and the latter are referred to as “OS-SART” and “TV-minimization”, respectively, throughout this paper. The OS-SART formula can be written as follows:

$$f_n^{(k+1)} = f_n^{(k)} + \gamma \sum_{m \in \Phi_b} \frac{\omega_{mn}}{\sum_{m' \in \Phi_b} \omega_{m'n}} \frac{p_{m,j} - \bar{W}_m \bar{f}^{(k)}}{\sum_{n=1}^N \omega_{mn}} \quad (2)$$

where  $k$  indicates the number of iterations;  $\bar{f}$  is the reconstructed image whose size is  $N = I \times J$  (in the current implementations,  $I$  equals  $J$ );  $p_{m,j}$  is the projection at the  $m$ th angle and  $j$ th detector position ( $J$  is the total size of detector);  $\gamma$  is relaxation parameter which was set to unity for simplicity;  $\Phi_b$  represents the set of ray indexes in the  $b$ th subsets;  $\bar{W}_m$  is the row of the system matrix, which is an improved distance-driven model [17]; and  $\omega_{mn}$  is an element of  $\bar{W}_m$ . The weighted method in the fast iterative shrinkage-thresholding algorithm [18] was employed to accelerate the convergence of the OS-SART.

TV-minimization can be defined as follows:

$$\left\| \vec{f} \right\|_{TV} = \sum_{i,j} \left| \vec{\nabla} f_{i,j} \right| = \sqrt{(f_{i,j} - f_{i-1,j})^2 + (f_{i,j} - f_{i,j-1})^2} \quad (3)$$

where  $\vec{\nabla}$  represents the local gradient operator and  $f_{i,j}$  is a pixel value of  $\bar{f}$  at position  $(i, j)$ .

The whole iteration process of TV-Minimization contains two loops; the outside loop operates OS-SART and the inside loop operates the TV gradient descent.

## 2.6. Image analysis

The CNR was determined by calculating the ratio of difference between the mean values (HU) of each region of interest (ROI) and the homogeneous PMMA background to the standard deviation of the background:

$$CNR = \frac{\bar{f}_{ROI} - \bar{f}_{BK}}{\sqrt{\sigma_{BK}^2}} \quad (4)$$

where  $\bar{f}_{ROI}$  and  $\bar{f}_{BK}$  are the mean values of the ROI and the background, respectively, and  $\sigma_{BK}^2$  is the variance of the background. According to the Rose criterion [6], a CNR of 5 is chosen to determine the detection limit. This chosen CNR value is also consistent with that used in a previous experimental study [19].

The modulation transfer function (MTF) relates the spatial resolution to the corresponding loss of contrast in the images and is defined as the Fourier transformation of the first derivative of the edge spread function (ESF) which is provided by the normalized intensity line profile [20]:

$$MTF = F \left\{ \frac{d}{dx} ESF(x) \right\} \quad (5)$$

## 2.7. Dose measurements

Dose measurements were performed in air using a Farmer-type ionization chamber (Model No. N30013, PTW) and an electrometer (Wellhofer DOSE 1 IBA Dosimetry). The dose rates were

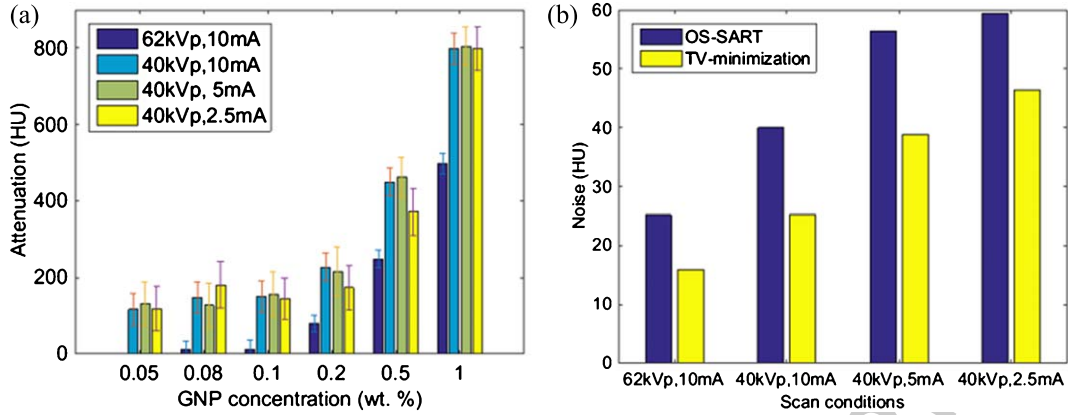


Fig. 2. Effect of x-ray tube voltages (40 kVp and 62 kVp), currents (2.5 mA, 5 mA, and 10 mA) and reconstruction algorithms (OS-SART and TV-minimization) on (a) attenuation of GNP solutions and (b) image noise (the standard deviation of the background) with 360 projections.

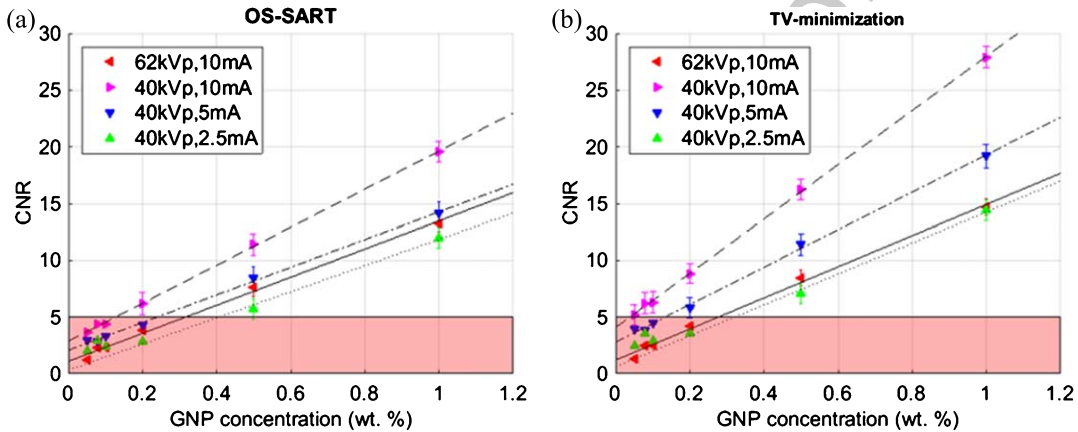


Fig. 3. Contrast-to-noise ratio (CNR) as a function of GNP concentration for various x-ray tube voltages (40 kVp and 62 kVp) and currents (2.5 mA, 5 mA, and 10 mA) using the (a) OS-SART and (b) TV-minimization method with 360 projections. The shaded area represents CNR < 5, which was considered to be below the detection threshold. The intersection of the linear fit with the shaded region represents the detection limit under that condition.

determined following the AAPM TG-61 formalism [21]. The doses delivered to the center of the phantom were obtained using the dose rates in air at the incident beam entry point (i.e., at 13.5 cm) and the depth dose data for the given beam spectra (i.e., 40 and 62 kVp x-rays filtered by 0.4 mm Al and 0.08 mm Cu)

### 3. Results

#### 3.1. Total projection reconstructions with various tube voltages and currents

The OS-SART and TV-minimization methods were used to do reconstructions with total projections (360 projections). Using the 3D printed GNP-loaded PMMA phantom, the attenuation (Fig. 2a), and the CNR (Fig. 3) were determined as a function of GNP concentration for various beam parameter settings (i.e., each x-ray tube voltage and current) and for each reconstruction algorithm studied. The noise (i.e., the standard deviation of the background) was also compared (Fig. 2b) under

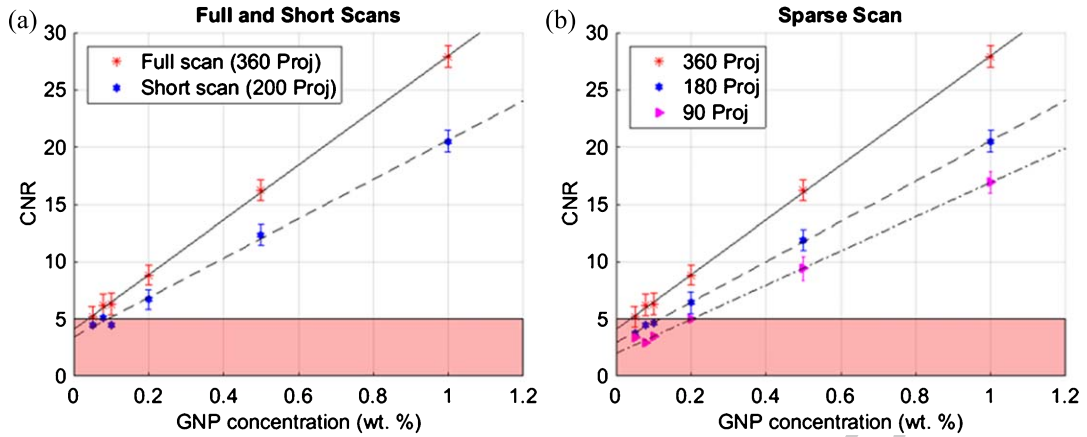


Fig. 4. Contrast-to-noise ratio (CNR) in the reconstructed image as a function of GNP concentration for 40 kVp and 10 mA. TV-minimization reconstruction results (a) for short ( $180^\circ$  plus the fan angle of  $20^\circ$ ) and full scans. (b) for sparse scans. The shaded area represents  $\text{CNR} < 5$ , which was considered to be below the detection threshold. The intersection of the linear fit with the shaded region represents the detection limit under that condition.

different scan conditions (x-ray tube voltage and current settings) and reconstruction methods (OS-SART and TV-minimization). As expected, for a given x-ray tube current (10 mA), attenuation and noise decreased with increasing voltage. As more photons passed through the phantom with 62 kVp compared to 40 kVp, there was less contrast and a smaller CNR. For a given x-ray tube voltage (40 kVp), we observed that, as expected, the attenuation produced for each current was very similar. However, noise decreased and CNR increased with increasing current. When images were reconstructed with TV-minimization compared with OS-SART, noise was reduced and CNR increased due to the smoothing effect of TV-minimization. Furthermore, CNR was increased linearly with GNP concentration.

### 3.2. Reconstructions of short and sparse scan results

Short and sparse scan approaches were tested under the 40 kVp and 10 mA setting. The images were reconstructed using TV-minimization. CNR values as a function of GNP concentration for short and sparse scans are shown in Fig. 4. As expected, CNR values were reduced as the number of projections for a given scan mode decreased. However, they did not change drastically, but remained similar (within  $\sim 10\%$ ) in both short (Fig. 4a) and sparse scans (Fig. 4b).

Depending on the given imaging scenarios, a balance between dose and image quality should be considered. Table 1 shows the detection limits (based on  $\text{CNR} > 5$ ) and x-ray dose under different scanning conditions. Corresponding reconstructed images are shown in Fig. 5. The detection limit of case (a) was 0.28 wt. %, but the x-ray dose was too high (11.74 cGy). The doses in cases (b)–(d) were 0.86 cGy, and the detection limit in case (d) was the smallest (0.2 wt. %). Overall, the image associated with case (f) was clearer than the rest of the cases. The GNP detection limit for case (f) was also the lowest among the considered cases. Apparently, these were direct consequences of a much larger dose (3.44 cGy) than other 40 kVp cases shown in Table 1. Nonetheless, x-ray dose for case (f) was significantly lower (by a factor of  $\sim 3$ ) than that for case (a) (based on the 62 kVp scan). Also, case (f) provided better contrast in the areas of low GNP concentrations (e.g., less than 1 wt. %) and lower detection limit than case (a) did.



Table 1

Detection limits (based on the detection threshold of  $CNR = 5$ ) and x-ray doses using TV – minimization under different scanning conditions. The results were based on either sparse or full scans

| Case | Voltage, kVp | Current, mA | No. of projections | Total exposure time, seconds | Detection limit, wt. % | Dose, cGy |
|------|--------------|-------------|--------------------|------------------------------|------------------------|-----------|
| (a)  | 62           | 10          | 360                | 6.12                         | 0.28                   | 11.74     |
| (b)  | 40           | 2.5         | 360                | 6.12                         | 0.32                   | 0.86      |
| (c)  | 40           | 5           | 180                | 3.06                         | 0.22                   | 0.86      |
| (d)  | 40           | 10          | 90                 | 1.53                         | 0.20                   | 0.86      |
| (e)  | 40           | 10          | 180                | 3.06                         | 0.12                   | 1.72      |
| (f)  | 40           | 10          | 360                | 6.12                         | 0.10                   | 3.44      |

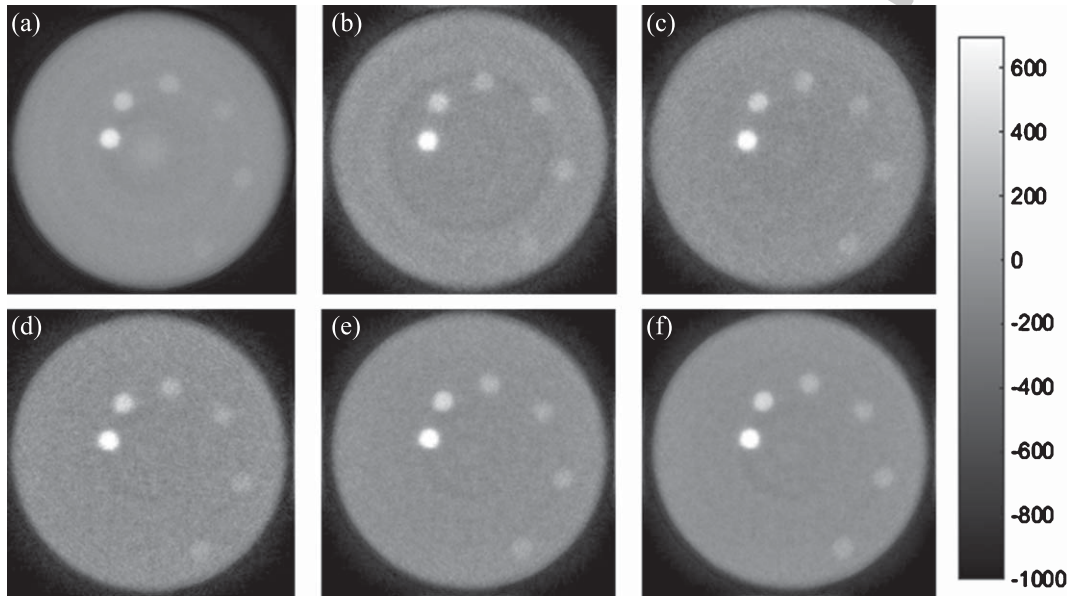


Fig. 5. Reconstructed images with a  $[-1000, 700]$  HU window under the corresponding conditions shown in Table 1.

### 3.3. System resolution and contrast

The image resolution phantom was scanned under 40 kVp and 10 mA conditions with different projections (360, 180 and 90) to get the system resolution. Figure 6 shows the reconstructed image (using TV-minimization), and the corresponding MTF as a function of LP/CM is shown in Fig. 7a. LPs in all the LP targets were separated in the images with 360 and 180 projections, whereas only the LPs within the 6 LP/CM target were separated in the image with 90 projections. As expected, MTF (50%) (Fig. 7b) decreased with decreasing numbers of projections. Images with 360, 180 and 90 projections yielded MTF (50%) of 9.5, 8.9 and 6.7 LP/CM respectively.

As shown in the previous section, 0.10 wt. % of GNPs were detectable (based on  $CNR > 5$ ) with a sufficiently low dose (3.44 cGy). The contrast (or attenuation) and noise for this case were 151 and 25 HU, respectively. The low-contrast phantom (containing targets 10 and 20 HU above the background) was also scanned, but no contrast was obtained as expected.



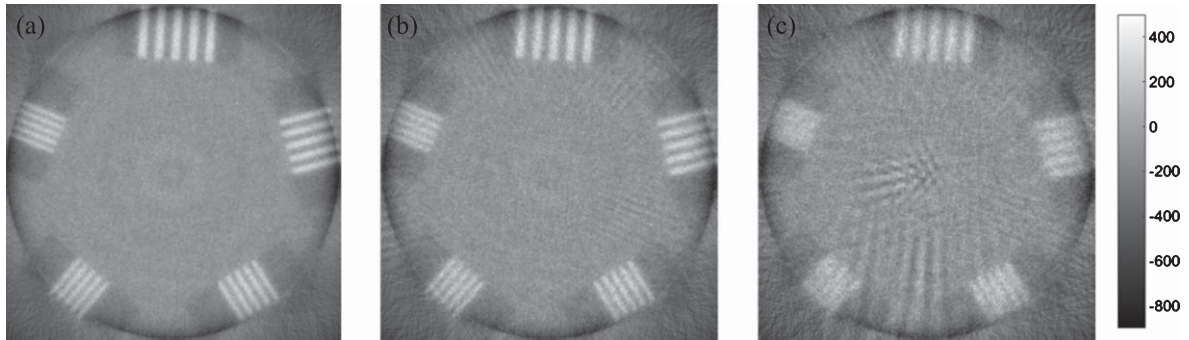


Fig. 6. Reconstructed image of resolution phantom with (a) 360, (b) 180, and (c) 90 projections. Images are shown within a  $[-900, 500]$  HU window. Note the data are presented up to the maximum LP/CM (i.e., 12) available from the phantom.

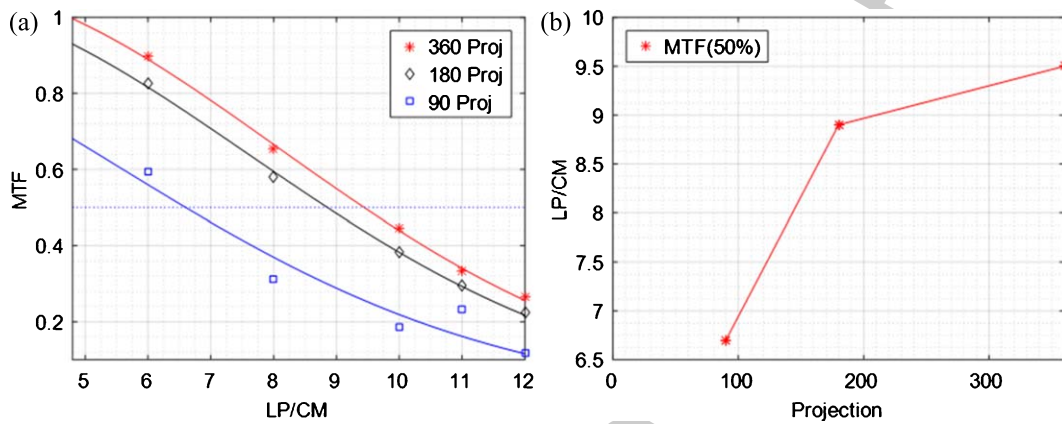


Fig. 7. Resolution phantom results: (a) Modulation transfer function (MTF) with 360, 180 and 90 projections as a function of line pairs (LP/CM) and (b) LP/CM corresponding to MTF (50%) as a function of projections. Note MTF is fit to a Gaussian function and the data are presented up to the maximum LP/CM (i.e., 12) available from the phantom.

#### 4. Discussion

We have shown in the current investigation that the CT component within our experimental benchtop XFCT system produced images deemed acceptable for multimodal imaging purposes, while requiring no more than 4 cGy of x-ray dose. These findings also suggest that it is possible to perform CT and XFCT scans sequentially with moderately increasing a total scan time for multimodal imaging purposes. For example, a CT scan of the currently used phantom with 360 projections can be completed in 18 minutes (3 seconds per projection inclusive of 17 ms x-ray exposure duration, detector readout and rotation of the object support stage), while the current experimental benchtop XFCT setup with a single detector would require up to one hour to complete an XFCT scan of the same phantom [14]. Note the XFCT scan time will become comparable to that of CT (e.g., on the order of 10 minutes), if the current benchtop XFCT system should be deployed with a pixelated or comparable 2D array detector [14]. It can also be noted that x-ray dose and CT scan time could be reduced further (e.g., 1.7 cGy and 9 minutes using 180 projections), if a slightly worse image resolution (e.g., 8.9 LP/CM instead of 9.5 LP/CM) was acceptable.

The current investigation provided results similar to previous studies [19, 22–24], but it did not immediately show whether the image quality from our system would be comparable to that of a typical microCT system. In principle, the system-level image resolution is strongly affected by the size of a

focal spot [20, 25]. Since the focal spot size of an x-ray tube used in the present study was 1 mm and larger than that of typical micro-focus x-ray tubes (less than 0.3 mm), the system-level image resolution was not as good as that of a microCT system. Nevertheless, as shown in this investigation, our system could produce an almost submillimeter image resolution (i.e., MTF (50%) in LP/CM is close to 10), partly due to the proximity of the panel x-ray detector to the imaging object.

In general, under the given condition (in terms of x-ray tube voltage, x-ray tube current, and x-ray dose), the CT image resolution achievable from our system is expected to be comparable to that reported in a previous study [24] for a commercially available small animal irradiator with CT capability. This is because of similarities between the two systems, especially in terms of the CT imaging geometry/instrumentation and the focal spot size of x-ray source. While not available from the current investigation, CBCT images of a mouse were acquired during the aforementioned study [24], showing the key organs and bony structures in sufficient details. Since these images were obtained under the conditions similar to those used for the current study, it is reasonable to expect comparable image resolution from our system, which would be acceptable for multimodal (CT + XFCT) imaging. Note the purposes of CT imaging within the current scope are mainly to allow for delineation of anatomical structures within a small animal as well as to provide a map of CT numbers for attenuation correction of relatively coarse XFCT images. Thus, it is not necessary to achieve a very high image resolution (e.g., on the order of a few 10s of LP/CM or more in MTF (50%)) typically available from a microCT system [20]. If any necessity for such a high image resolution arose, one would consider hardware upgrades such as adopting a high power micro-focus x-ray source and a panel detector with smaller pixel pitch as well as further optimization of CBCT imaging geometry.

As shown earlier, our system could not produce any contrast for a commercial low-contrast CT QA phantom. According to a previous study [26], the HU of Alderson lung, Alderson muscle (composition A), adipose tissue, skeleton yellow marrow and skeleton cortical bone at 30 keV (the mean photon energy of filtered 40 kVp x-rays from our system) are -744, -202, -227, -215 and +5791, while that of soft tissue is +68. Thus, the contrasts between the listed lung/muscle/tissue/marrow/bone and soft tissue are all more than 270 HU, which is well above the minimum detectable contrast of our system (151 HU) as determined using our GNP-loaded spiral phantom. However, it is important to note that the results obtained in this study were derived from the scanning of relatively simple phantoms. The results from scanning small animals might be somewhat different and also influenced by various factors including possible organ motion/animal movement, air pockets presented in the anatomy, and the presence of contrast agents (other than GNPs). These issues are beyond the scope of the current study but can be investigated in future animal imaging studies.

In addition to the unique factors for integrating CT with XFCT imaging as discussed above, several other factors related to CT imaging are important to mention. One of such factors is the algorithm used for the CT image reconstruction. In a previous study [27], the filtered backprojection [28] method was used to produce CT images with Monte Carlo data. In another published study [29], the maximum likelihood method with expectation maximization [30] was used to reconstruct CT images with numerically-derived data. In a recent study [31], iterative reconstruction techniques and model-based reconstruction were used to produce CT images with Philips Brilliance iCT scanner data. In our study, OS-SART with the TV-minimization constraint, which has been shown to provide faster reconstruction speed and better sparse representation, was used to reconstruct CT images. As a projection matrix operator, the improved distance-driven model, which was used in our study, has also been demonstrated to have better performance than the pixel-driven model [32], ray-driven model [33], distance-driven model [34, 35], and area-integral model [36]. This algorithm is currently unavailable in commercial CT scanners and requires the system information, which might be different among the CT scanners. However, these limitations will likely diminish with future developments and updates in commercial CT scanners.

## 5. Conclusion

For the case (40 kVp, 10 mA, 360 projections) that provided the best contrast in this study, the GNP detection limit (based on CNR > 5) and LP/CM corresponding to MTF (50%) were 0.10 wt. % and 9.5 LP/CM, respectively. The noise for the image resulting in the lowest GNP detection limit was 25 HU. The CT dose corresponding to the aforementioned case was 3.44 cGy. Considering these results, the CT component within the current experimental benchtop CT + XFCT system can be used for multimodal CT + XFCT imaging with sufficiently low x-ray dose (<4 cGy), while providing the image resolution deemed acceptable for preclinical imaging studies. Overall, the current investigation provides valuable insights into the development of a dual-mode benchtop CT + XFCT system for multimodal preclinical imaging purposes.

## Acknowledgments

This investigation was supported by the US National Institutes of Health under the award number R01EB020658. The content is solely the responsibility of the authors and does not necessarily represent the official views of the US National Institutes of Health. L.D. was supported by the Graduate Scientific Research and Innovation Foundation of Chongqing, China (grant no. CYB16044) and the China Scholarship Council. P.F. and B.W. were supported by the Fundamental Research Funds for the Central Universities (No. 2018CDGFGD0008). The authors acknowledge Yeonok Park, PhD and Erica Goodoff, ELS at The University of Texas MD Anderson Cancer Center for assistance with CT imaging and editorial help with the manuscript, respectively.

## Disclosure of conflicts of interest

The authors have no relevant conflicts of interest to disclose.

## References

- [1] S.K. Cheong, B.L. Jones, A.K. Siddiqi, F. Liu, N. Manohar and S.H. Cho, X-ray fluorescence computed tomography (XFCT) imaging of gold nanoparticle-loaded objects using 110 kVp x-rays, *Phys Med Biol* **55** (2010), 647–662.
- [2] J.M. Boone, O. Velazquez and S.R. Cherry, Small-animal X-ray dose from micro-CT, *Mol Imaging* **3** (2004), 149–158.
- [3] P.L. Chow, A.L. Goertzen, F. Berger, J.J. DeMarco and A.F. Chatziioannou, Monte Carlo model for estimation of dose delivered to small animals during 3D high resolution X-ray computed tomography. Nuclear Science Symposium Conference Record, 2001 IEEE: IEEE; 2001. pp. 1678–1681.
- [4] A. Obenaus and A. Smith, Radiation dose in rodent tissues during micro-CT imaging, *Journal of X-ray Science and Technology* **12** (2004), 241–249.
- [5] N. Manohar and S.H. Cho, Quality of micro-CT images acquired from simultaneous micro-CT and benchtop x-ray fluorescence computed tomography (XFCT): A preliminary Monte Carlo study. Nuclear Science Symposium and Medical Imaging Conference (NSS/MIC), 2013 IEEE: IEEE; 2013. pp. 1-3.
- [6] A. Rose, Vision: Human and electronic. Applied Solid State Physics: Springer; 1970. pp. 79–160.
- [7] D. Dickerscheid, J. Lavalaye, L. Romijn and J. Habraken, Contrast-noise-ratio (CNR) analysis and optimisation of breast-specific gamma imaging (BSGI) acquisition protocols, *EJNMMI Res* **3** (2013), 9.
- [8] A. Naparstek, Short-scan fan-beam algorithms for Cr, *IEEE Trans Nucl Sci* **27** (1980), 1112–1120.
- [9] F. Noo, M. Defrise, R. Clackdoyle and H. Kudo, Image reconstruction from fan-beam projections on less than a short scan, *Physics in Medicine and Biology* **47** (2002), 2525.
- [10] D.L. Parker, Optimal short scan convolution reconstruction for fanbeam CT, *Medical Physics* **9** (1982), 254–257.
- [11] E.Y. Sidky and X. Pan, Image reconstruction in circular cone-beam computed tomography by constrained, total-variation minimization, *Physics in Medicine and Biology* **53** (2008), 4777–4807.

- [12] E.Y. Sidky, C-M. Kao and X. Pan, Accurate image reconstruction from few-views and limited-angle data in divergent-beam CT, *Journal of X-ray Science and Technology* **14** (2006), 119–139.
- [13] D.L. Donoho, Compressed sensing, *IEEE Trans Inf Theory* **52** (2006), 1289–1306.
- [14] N. Manohar, F.J. Reynoso and S.H. Cho, A benchtop cone-beam x-ray fluorescence computed tomography (XFCT) system with a high-power x-ray source and transmission CT imaging capability, *Medical Physics* **45** (2018), 4652–4659.
- [15] M.F. Ahmed, S. Yasar and S.H. Cho, A Monte Carlo Model of a Benchtop X-Ray Fluorescence Computed Tomography System and Its Application to Validate a Deconvolution-based X-Ray Fluorescence Signal Extraction Method, *IEEE Trans Med Imag* **37**(11) (2018), 2483–2492.
- [16] G. Wang and M. Jiang, Ordered-subset simultaneous algebraic reconstruction techniques (OS-SART), *Journal of X-ray Science and Technology* **12** (2004), 169–177.
- [17] C. Miao, B. Liu, Q. Xu and H. Yu, An improved distance-driven method for projection and backprojection, *Journal of X-ray Science and Technology* **22** (2014), 1–18.
- [18] A. Beck and M. Teboulle, A fast iterative shrinkage-thresholding algorithm for linear inverse problems, *SIAM J Imaging Sci* **2** (2009), 183–202.
- [19] D.P. Clark, K. Ghaghada, E.J. Moding, D.G. Kirsch and C.T. Badea, In vivo characterization of tumor vasculature using iodine and gold nanoparticles and dual energy micro-CT, *Physics in Medicine and Biology* **58** (2013), 1683–1704.
- [20] J. Rueckel, M. Stockmar, F. Pfeiffer and J. Herzen, Spatial resolution characterization of a X-ray microCT system, *Appl Radiat Isot* **94** (2014), 230–234.
- [21] C.M. Ma, C. Coffey, L. DeWerd, C. Liu, R. Nath, S. Seltzer, et al., AAPM protocol for 40–300kV x-ray beam dosimetry in radiotherapy and radiobiology, *Medical Physics* **28** (2001), 868–893.
- [22] J. Hainfeld, D. Slatkin, T. Focella and H. Smilowitz, Gold nanoparticles: A new X-ray contrast agent, *The British Journal of Radiology* **79** (2006), 248–253.
- [23] J.F. Hainfeld, M.J. O'Connor, F. Dilmajian, D.N. Slatkin, D.J. Adams and H.M. Smilowitz, Micro-CT enables microlocalisation and quantification of Her2-targeted gold nanoparticles within tumour regions, *The British Journal of Radiology* **84** (2011), 526–533.
- [24] R. Clarkson, P. Lindsay, S. Ansell, G. Wilson, S. Jelveh, R. Hill, et al., Characterization of image quality and image-guidance performance of a preclinical microirradiator, *Medical Physics* **38** (2011), 845–856.
- [25] S. Vedantham, S. Shrestha, A. Karellas and S.H. Cho, A framework for optimizing micro-CT in dual-modality micro-CT/XFCT small-animal imaging system. Radiation Detectors in Medicine, Industry, and National Security XVIII: International Society for Optics and Photonics; 2017. pp. 103930R.
- [26] I. ICRU, Tissue substitutes in radiation dosimetry and measurement. International Commission on Radiation Units and Measurements. 1989.
- [27] M. Bazalova, Y. Kuang, G. Pratz and L. Xing, Investigation of x-ray fluorescence computed tomography (XFCT) and K-edge imaging, *IEEE Transactions on Medical Imaging* **31** (2012), 1620–1627.
- [28] S. Zhang, W. Li and G. Tang, Study on image reconstruction algorithm of filtered backprojection, *Journal of Xianyang Normal University* **23** (2008), 47–49.
- [29] P. Feng, W. Cong, B. Wei and G. Wang, Analytic comparison between X-ray fluorescence CT and K-edge CT, *IEEE Trans Biomed Eng* **61** (2014), 975–985.
- [30] L.A. Shepp and Y. Vardi, Maximum likelihood reconstruction for emission tomography, *IEEE Trans Med Imaging* **1** (1982), 113–122.
- [31] A.L. Bernstein, A. Dhanantwari, M. Jurcova, R. Cheheltani, P.C. Naha, T. Ivanc, et al., Improved sensitivity of computed tomography towards iodine and gold nanoparticle contrast agents via iterative reconstruction methods, *Scientific Reports* **6** (2016), 26177.
- [32] G.T. Herman, Image reconstruction from projections, *Real-Time Imaging* **1** (1995), 3–18.
- [33] G. Zeng and G. Gullberg, Ray-driven backprojector for backprojection filtering and filtered backprojection algorithms. Proceedings of the 1993 IEEE Nuclear Science Symposium & Medical Imaging Conference: Publ by IEEE; 1994.
- [34] B. De Man and S. Basu, Distance-driven projection and backprojection in three dimensions, *Physics in Medicine and Biology* **49** (2004), 2463.
- [35] B. De Man and S. Basu, Distance-driven projection and backprojection, *Nuclear Science Symposium Conference Record, 2002 IEEE: IEEE*; 2002. pp. 1477–1480.
- [36] H. Yu and G. Wang, Finite detector based projection model for high spatial resolution, *Journal of X-ray Science and Technology* **20** (2012), 229–238.